REPORT
doi:10.26443/seismica.v5i2.3013

# 2023 Kīlauea Horizontal-Component Signal/Noise Assessment of a Large Three-Component Nodal Array

**Daniel R.H. O'Connell** * [1], **Aaron J. Girard** [2]

[1]Tetra Tech, Lakewood, CO 80401, USA, [2]Colorado School of Mines, Golden, CO 80401, USA

Author contributions: *Conceptualization*: Daniel R.H. O'Connell. *Methodology*: Daniel R.H. O'Connell. *Software*: Daniel R.H. O'Connell. *Formal Analysis*: Daniel R.H. O'Connell and Aaron J. Girard. *Investigation*: Daniel R.H. O'Connell. *Writing - Original draft*: Daniel R.H. O'Connell. *Writing - Revision*: Aaron J. Girard. *Visualization*: Daniel R.H. O'Connell.

**Abstract** In spring 2023, 1,802 three-component seismic nodes were deployed over a 13 × 13 km area within and around Kīlauea Caldera, Hawai'i. The continuous recordings include vibroseis signals from 396 source positions and more than 12,000 detected and located earthquakes. Three node types were installed across pāhoehoe and 'a'ā lava flows, volcanic tephra, and dense jungle. Because permits precluded burial, all nodes were surface-deployed and exposed to persistent trade winds. We use horizontal-to-vertical spectral ratios (H/V) to assess horizontal-component signal-to-noise ratio (S/N) as functions of frequency and wind speed, and to quantify how node geometry and deployment configuration affect wind sensitivity. Taller, narrower spike-mounted nodes are more susceptible to wind-induced rocking than shorter, wider nodes on leveling legs. Volcanic tremor produces strong horizontal noise at 1–5 Hz. Vibroseis sweeps were limited to frequencies >5 Hz, constraining weak S-wave detection to the same band, where wind-driven horizontal noise is often highest. We provide H/V estimates for all node data and for 12 United States Geological Survey (USGS) Hawaii Volcano Observatory (HVO) network stations. Based on H/V S/N estimates, we identify four station subsets: three suitable for earthquake and active-source S-wave detection and picking, and one of 1,099 stations suitable for lower-frequency (<1.2 Hz) interferometry.

**Non-technical summary** In spring 2023, scientists installed 1,802 portable seismometers around the summit of Kīlauea volcano in Hawai'i to record ground shaking over several weeks, capturing more than 12,000 earthquakes and signals from a large vibrating-truck source, in a period that ended with a new eruption. Deploying this many instruments at an active volcano is rare, and the recordings are freely available for others to study how the volcano and its earthquakes behave. Park rules did not permit burying the instruments, so they sat on the ground surface, where strong, near-constant trade winds rocked them and added noise that is especially troublesome on the sideways-shaking channels that many analyses depend on. We measured how strongly wind affected each instrument, how this depended on the instrument's shape and how it was installed, and then identified which instruments, and which sites, recorded trustworthy data. The outcome is practical guidance: lists of the best stations to use for different types of analysis, and recommendations for installing instruments on the surface when burial is not possible, so that this large public dataset can be used effectively and future field campaigns can plan around wind.

Production Editor:
Gareth Funning
Handling Editor:
Oliver Lamb
Copy & Layout Editor:
Hannah F. Mark

Received:
April 23, 2026
Accepted:
August 24, 2026
Published:
September 10, 2026

## 1 Introduction

In spring 2023, 1,802 three-component (3C) continuous recording seismic nodes were deployed over a 13 × 13 km area within and around the Kīlauea caldera in Hawai'i Volcanoes National Park; the node data are publicly available (Denlinger et al., 2023). The recordings include vibroseis signals from 396 source positions (144 with triaxial sourcing). United States Geological Survey (USGS) Hawaii Volcano Observatory (HVO) network stations and deployed nodes detected and located over 12,000 earthquakes (Roecker et al., 2026). Deployment permits precluded node burial, allowing persistent trade winds to rock the sensors and degrade the horizontal-component recordings used in many seismic analyses. Processing is complicated by multiple strong noise sources in the 0.1–40 Hz band, wind sensitivity of some nodes, and ground-motion decoupling at a small subset of stations. Nevertheless, subsets of stations exhibit relatively high horizontal-component signal/noise ratio (S/N) within useful frequency bands, and identifying them is the goal of this study.

Three-component nodes are increasingly used in seismology, and many target analyses depend on horizontal-component data: teleseismic receiver functions that jointly use horizontal and vertical channels (Ward and Lin, 2017), dense-array local seismicity and crustal imaging (Schmandt and Clayton, 2013; Trow et al., 2018), active-source imaging (Parker et al., 2018), ambient-noise interferometry and surface-wave imaging (Obermann et al., 2022), and the broader range of large-N geophone-array applications (Karplus and Schmandt, 2018). Horizontal-component quality is,

*Corresponding author: geomgcn@gmail.com

however, strongly affected by sensor coupling, burial, and wind, and existing performance characterizations have largely examined a single instrument type under controlled or limited conditions (Ringler et al., 2018; Johnson et al., 2019; Farrell et al., 2018; Dean and Grant, 2024). The closest prior comparison is Janiszewski et al. (2024), who assessed 80 surface-deployed SmartSolo IGU-BD3C-5 nodes, coupled with sandbags rather than spikes or burial, against many of the same HVO permanent stations used here. The 2023 Kīlauea deployment is distinctive in co-locating several surface-deployed node designs alongside permanent HVO broadband sensors under a common, persistently windy setting. This combination motivates a horizontal-component signal/noise assessment built specifically for this dataset, so that the station subsets and frequency bands appropriate to each analysis can be identified across the different instrument packages rather than assumed from any one sensor type.

Horizontal-to-vertical spectral ratios (H/V) are used to assess horizontal-component S/N and to define four node subsets with progressively improved horizontal-component S/N as fewer nodes are retained, each usable over a target frequency band. One subset, usable to 1.2 Hz, supports interferometry; the other three, usable to at least 10 Hz, support earthquake and active-source S-wave arrival-time picking, moment-tensor analysis, and S-wave attenuation tomography. High-quality H/V data provide constraints on shallow S-wave velocities. Frequency-dependent estimates of H/V S/N are required for effective use of H/V in tomographic inversions for shallow S-wave velocities. This study provides a qualitative guide to horizontal-component and H/V S/N to support analyses using this publicly available dataset.

During the 2023 Kīlauea 3D data acquisition period (late April to early June 2023), Kīlauea caldera underwent magma inflation that produced strong volcanic tremor that often dominated horizontal-component signals in the 1–5 Hz band. This episode culminated in the June 7, 2023 lava eruption in the western portion of Halemaʻumaʻu crater within Kīlauea caldera. The 30,400 kg T-REX triaxial vibroseis source could only operate at frequencies >5.0 Hz due to hydraulic-mechanical and vibroseis controller limitations, with most vibroseis sweeps confined to downsweeps in the 5.0–27.0 Hz band. Consequently, for both earthquake and vibroseis data, the best S-wave S/N from smaller-magnitude earthquakes and active sourcing is confined to frequencies >5.0 Hz. Strong trade winds persisted over nearly the entire duration of full node deployment. H/V results indicate that wind noise often dominated high-frequency horizontal-component signals starting at frequencies between 1 and 4 Hz on many 3C nodes. In addition, 394 nodes were deployed on lava flows directly exposed to wind, where burial was not physically feasible.

Three types of 3C nodes were deployed to suit the varied ground conditions: some nodes were leveled on hard, irregular lava surfaces and others placed on soil and volcanic tephra. 152 Geophysical Technology Incorporated (GTI) U3 2 Hz 3C nodes (GTI U3 2 Hz nodes, Geophysical Technology, Inc., 2026) were designed for and deployed on lava surfaces with leveling legs. The Hawaii Volcano Observatory (HVO) provided 71 SmartSolo (SS) IGU-BD3C-5 0.2 Hz nodes (HVO SS 0.2 Hz nodes, SmartSolo Inc., 2026b) with leveling legs for deployment on lava surfaces. The EarthScope Instrument Center (EPIC, formerly IRIS PASSCAL) provided 1579 SS 3C IGU-16HR-3C 5 Hz nodes (SmartSolo Inc., 2026a); data were recovered from 1576 of these nodes. 167 of these EPIC SS 5 Hz 3C nodes were deployed in 5-gallon plastic buckets half-filled with low-density coral sand (bucket nodes) to enable coverage of accessible lava-flow surfaces in the project area. The long central spike was removed before placement in buckets, and the nodes were glued to the bucket bottoms with rope caulk before half-filling the buckets with the sand. Consequently, the horizontal-component performance of each node type and deployment configuration is essential for effective use of these data in H/V analyses, S-wave arrival-time picking, and interferometry and is the focus of this paper.

## 2 Calculation of H/V

Horizontal-component performance of surface-deployed sensors is commonly assessed through power spectral density and probabilistic PSD comparisons against reference noise models (Peterson, 1993), through co-located tests against a reference sensor, through three-channel coherence analysis for instrument self-noise, or through direct correlation with co-located anemometry (Dybing et al., 2019). H/V was used here for three reasons. The calculations require neither a co-located reference sensor nor an absolute calibration, which is a practical necessity for an array of 1,799 instruments deployed without co-located references. They also normalize source and path effects common to all three components, so that what remains is the horizontal-to-vertical difference in which wind-induced rocking appears. And lastly, they also yield shallow site-response information as a byproduct. The principal limitation is that H/V alone cannot distinguish a genuine site resonance from a coupling or spike resonance at the same frequency; the wind-speed conditioning introduced in Section 5 is what separates the two, because a coupling resonance grows with wind speed and a site resonance does not. H/V was calculated from 59 windows of length 61.43 s extracted from each available 61-minute Seismic Analysis Code (SAC) file for each node. Each SAC file starts on the hour. Additionally, H/V was calculated for subsets of full hours spanning a range of wind speeds to assess wind-speed effects on H/V and horizontal-component S/N. The SAC files have a 0.01 s sampling interval derived from the original 0.004 s interval using an antialiasing corner frequency of 40 Hz and a low-pass windowed-sinc filter (Smith, 1998) prior to decimation and sinc interpolation. The EPIC SS 5 Hz node and GTI U3 2 Hz node data were corrected for individual geophone responses based on step calibration self-testing logs and remapped to have 0.2 Hz geophone responses. This sometimes amplified low-frequency noise and produced long-period drift in subsets of nodes. Data were not demeaned or high-pass filtered prior to tapering; another goal of this investigation was to determine the low-frequency limits of useful S/N for each node type. Individual component multitaper spectra were calculated using five orthogonal Slepian tapers (Thomson, 1982; Lees and Park, 1995). Hourly ln-mean H/V and standard deviations were calculated for each component from 20% alpha-trimmed hourly H/V. Station-level summary ln-mean H/V and standard deviations were then computed from all available hourly data. These H/V results were combined with additional H/V analyses from subsets of hours, where steady trade winds were $<0.8$ m/s, $<1.6$ m/s, equal to 4.6 m/s (median wind speed), and $>6.6$ m/s to assess H/V S/N stability and frequency bandwidth as a function of wind speed.

## 3 Predictive Characterization of Each Node's Wind Sensitivity

This analysis evaluates how node shape and deployment configuration affect wind-induced noise on horizontal components and associated H/V. Persistent trade winds impinge on Volcano (northeast of the deployment area; Fig. 1) from the east to northeast (Garza et al., 2012) and typically sweep southwest across the array. Mean wind speeds from April to June are 4.6 m/s at Volcano, decreasing to 3.6 m/s at Hilina Pali Road, marked in Fig. 1 on the southwest side of the deployment area. Stations with calculated H/V are shown in map view in Fig. 1.

Seismic node manufacturers generally agree that the best deployment method to minimize noise is to bury nodes, with most nodes designed to receive adequate GPS signals even when buried beneath 2–4 cm of soil. For some seismic nodes, burial is the sole manufacturer-recommended method of deployment. Poor coupling between a surface-deployed sensor and the ground allows the instrument to rock under wind and ambient loading, which degrades the horizontal components and is a primary reason burial is recommended (Dean et al., 2018). For compact 3C nodes this rocking produces a coupling resonance within the seismic band that appears preferentially on the horizontal components as an anomalous peak in spectral ratios (Dean and Grant, 2024), and is therefore particularly relevant for analyses requiring reliable spectra, such as H/V. Consistent with this, the SmartSolo IGU-16HR-3C is specified for buried deployment to improve coupling (SmartSolo Inc., 2026a); because permits precluded burial here, the resulting horizontal-component resonance is documented across the array in Section 4. Such behavior is not particular to volcanic or Hawaiian settings: Dybing et al. (2019) document wind-induced noise on near-surface broadband sensors across a range of non-volcanic sites, and Dean and Grant (2024) report the coupling resonance for compact three-component nodes under controlled conditions.

The Kīlauea deployment of 1,576 EPIC SS 5 Hz 3C nodes provides a large sample for characterizing these coupling and wind-noise effects on spiked surface deployments. Accordingly, EPIC SS 5 Hz node H/V results from Kīlauea provide a basis to evaluate wind-noise effects for spiked surface deployments relative to the shorter HVO SS 0.2 Hz and GTI U3 2 Hz 3C nodes, which have horizontal-component geophones located in the lower portion of the housing (Fig. 2). Of the 1,802 deployed 3C nodes, data were recovered and H/V estimated from 1,799 nodes, comprising 1,409 EPIC SS 5 Hz spiked nodes, 167 EPIC SS 5 Hz bucket nodes, and 152 GTI U3 2 Hz nodes (3C H/V data from 150 of 152 GTI nodes; two nodes had horizontal-geophone failure), plus 71 HVO SS 0.2 Hz nodes. Three nodes were lost or destroyed. Details and dimensions of the EPIC SS 5 Hz spiked node (Fig. 2a), the HVO SS 0.2 Hz node (Fig. 2b), and the GTI U3 2 Hz node (Fig. 2c) are summarized in Table 1. The fourth node configuration consisted of EPIC SS 5 Hz 3C bucket nodes, deployed in covered 5-gallon plastic buckets half-filled with coral sand.

Node dimensions are from manufacturers' datasheets (Table 1); Fig. 2 shows photographs and schematics indicating geophone locations within each node type.

Relative wind sensitivity is defined as the ratio of node height to half the node base width (or the distance from node center to the leveling-leg contact points), as a proxy for relative wind-induced torque about the vertical axis. For EPIC SS nodes, rocking resistance is provided mainly by the long, central spike (spiked deployments) or surrounding coral sand (bucket deployments); for HVO SS and GTI U3 nodes, resistance is governed mainly by leveling-leg spacing. Rocking in response to wind loading primarily increases noise on the horizontal-component geophones.

Table 2 lists relative wind-sensitivity estimates for horizontal-component noise. Additional influences not captured by Table 2 include: (1) GTI U3 leveling bolts were updated to M10 bolts with flat tips (rather than pointed tips), increasing ground contact area from a point to an approximately 1 cm-wide contact and increasing rocking resistance relative to HVO SS nodes, which retained pointed-tip leveling legs; and (2) tapered spikes (as used on the EPIC SS nodes) can loosen over time after installation. In low-cohesion substrates with minimal sticky clay (e.g., volcanic tephra), an upward ground reaction associated with spike taper can reduce coupling over time and increase susceptibility to wind-driven rocking.

Although wind speed is the primary variable considered, other factors can contribute to rocking motions and elevated horizontal-component noise. Many lava flows were platy; surficial plates commonly flaked during site preparation, complicating efforts to establish stable, repeatable ground contact at leveling points. As a result, some lava flow sites likely exhibited spurious resonances associated with irregular contact at one or more leveling legs. On irregular hard surfaces, bucket placement to maintain consistent node orientation and level was also difficult. These effects are not quantified here.

Wind-sensitivity ratios in Table 2 provide first-order predictions of node H/V amplification relative to the

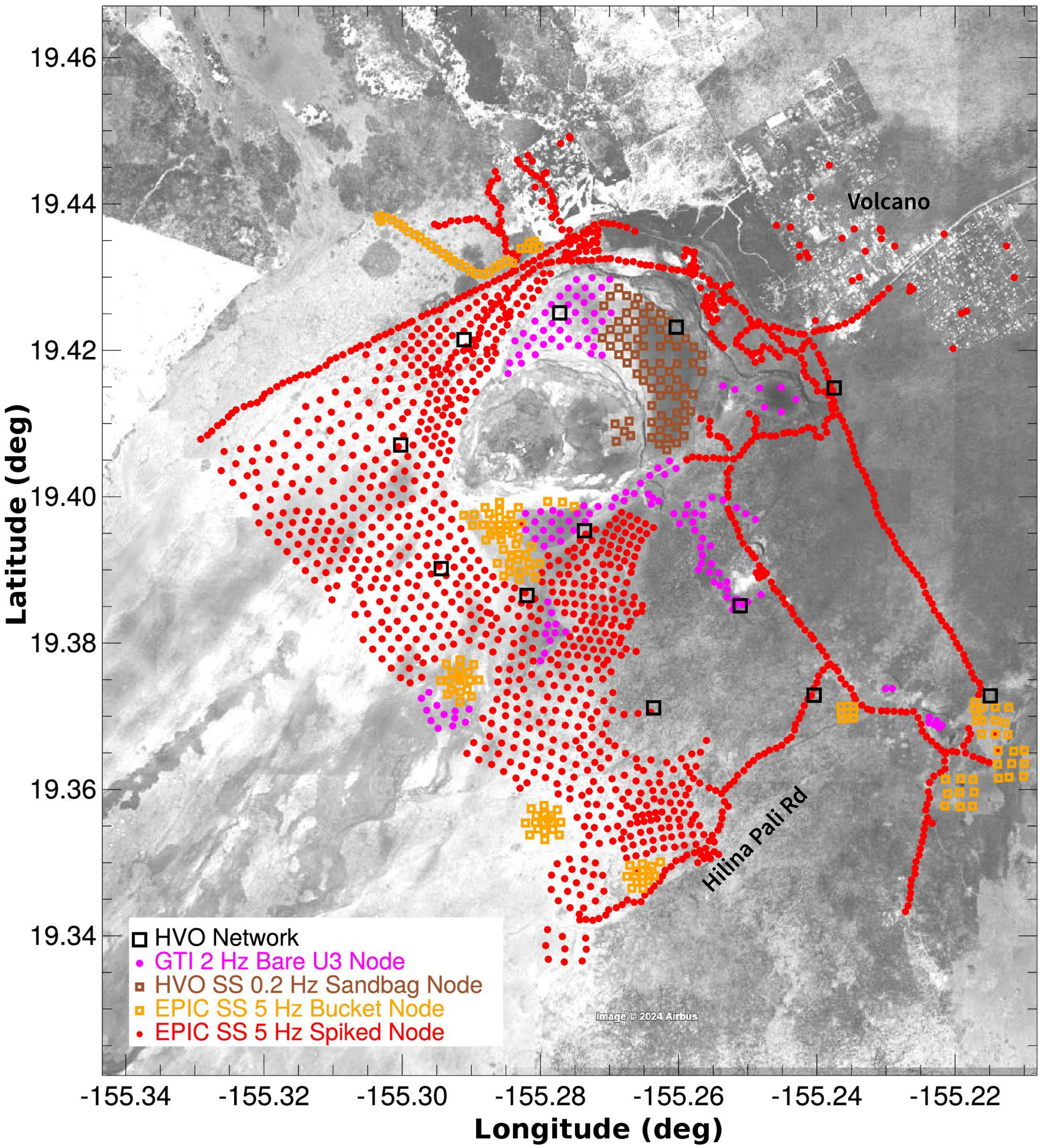


**Figure 1** Map with gray-scaled imagery showing the locations of 3C seismographic stations with H/V estimates that operated during the 2023 Kīlauea 3C nodal deployment, symbol- and color-coded as per the legend. The Kīlauea caldera occupies the north-central portion of the map, with GTI U3 2 Hz nodes in the northern part of the caldera floor and HVO SS 0.2 Hz nodes located in the northeastern and eastern parts of the Kīlauea caldera floor; five of these nodes were deployed on the highest eastern block of Halemaʻumaʻu crater.

permanent HVO network stations. These predictions are evaluated by comparing node and network H/V values calculated from all available complete hours of data. These ratios are geometric and do not account for substrate stiffness, spike-substrate interaction, or local wind exposure, all of which vary across the deployment area and modulate the observed response. Accordingly, the ratios are intended to rank configurations by susceptibility rather than to predict absolute noise levels or the frequencies at which wind noise becomes limiting, both of which depend on site conditions and on the local wind regime. The comparisons in Sections 5 and 6 provide some bound on the size of that modulation, since deployment areas differing substantially in

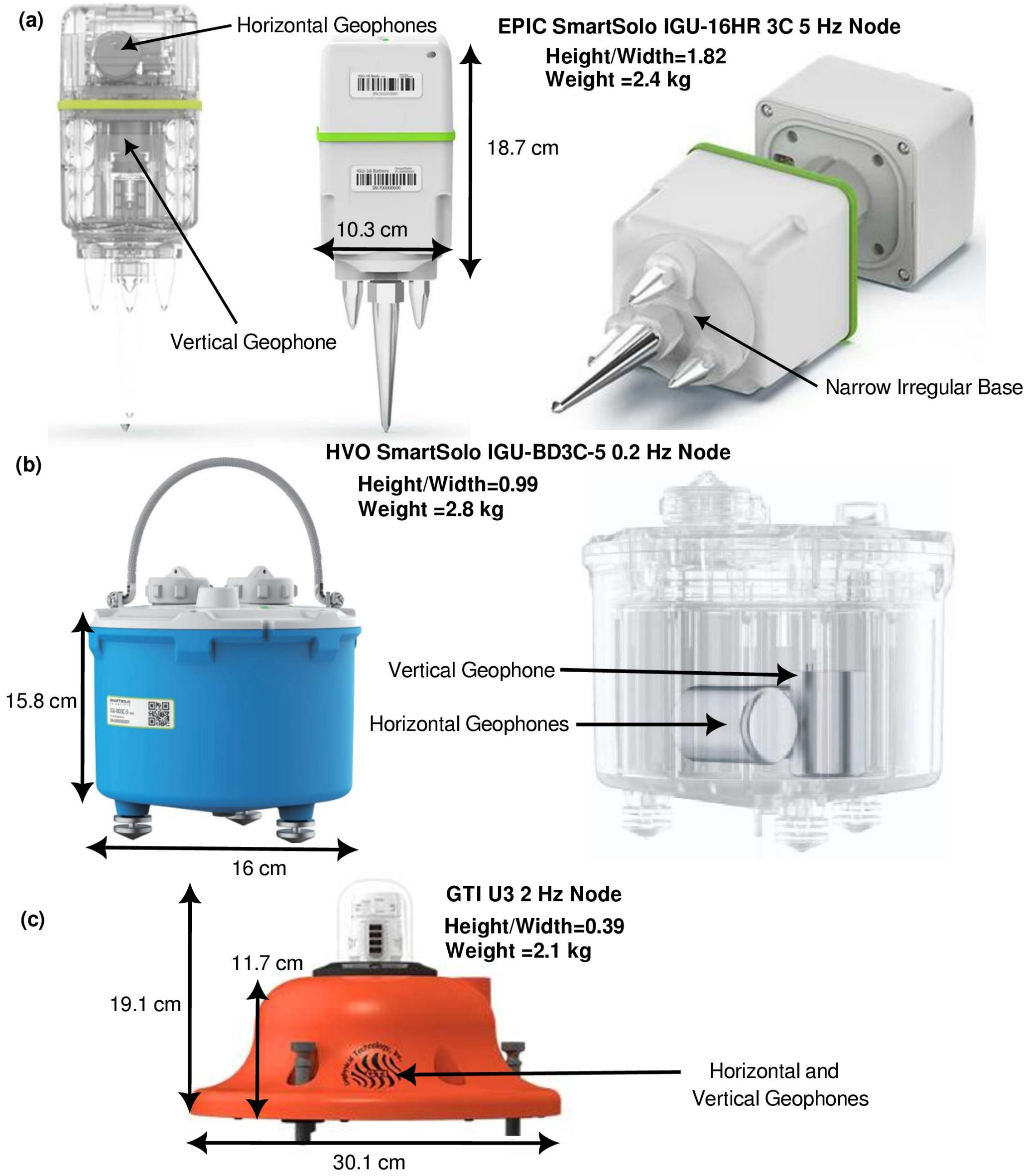


**Figure 2** (a) Photographs of the EPIC SmartSolo IGU-16HR 3C 5 Hz node (EPIC SS 5 Hz node) and a schematic showing internal geophone positions. The long central spike was removed for bucket deployment, leaving a $\sim$1 cm center-threaded stud protruding from the bottom of the node. (b) Photograph of the SmartSolo IGU-BD3C-5 HVO 0.2 Hz node (HVO SS 0.2 Hz node) and a schematic showing internal geophone positions. A rectangular sandbag was draped across the top of the node during deployment (not shown). (c) Photograph of the GTI U3 2 Hz node; the geophones are installed on the floor of the internal cavity. Node images reproduced with permission of the manufacturers (SmartSolo Inc., 2026a,b; Geophysical Technology, Inc., 2026). 

| Node | Height[a] (cm) | Width (cm) | Center-of-Mass Height[b] (cm) | Half Base Width[c] (cm) | Shape |
|---|---|---|---|---|---|
| EPIC SS | 18.7 | 13 | 13 | 3.7 | rectangular |
| HVO SS | 15.8 | 16 | $>5$ | 5.6 | cylindrical[d] |
| GTI U3 | 11.7 | 30.1 | 5 | 11 | cylindrical |

**Table 1** Node characteristics. [a]Height from base to the top of the node; for GTI U3, height is from the top to the base of the case (the Lexan cap assembly is very light). [b]Center of mass is approximate; it may be up to twice the listed height for HVO SS nodes due to sandbags placed on top of the nodes. [c]Distance from the center to the leveling-screw contact points for HVO SS and GTI U3 nodes; EPIC SS is smaller due to vertical and horizontal irregularities of the base (see Fig. 2). [d]Rectangular sandbags eliminate cylindrical symmetry of HVO SS nodes.

exposure and substrate preserve the ordering of node types predicted here. The proxy has not been evaluated for substrates outside the range sampled in this deployment or for wind regimes with different mean speeds and variability.

| Node | Height Wind Sensitivity[d] | Center of Mass Wind Sensitivity[e] | Wind Resistance |
|---|---|---|---|
| EPIC SS | 5.1 | 3.51 | half base width |
| HVO SS | >2.82 | >0.89 | leveling legs offset |
| GTI U3 | 1.06 | 0.45 | leveling legs offset |

**Table 2** Relative wind sensitivity from node characteristics. These ratios are geometric torque proxies (node height divided by half the base width) that rank the surface-deployed node types by susceptibility to wind-induced rocking; the permanent HVO network stations are not part of this geometric scale. In the H/V comparison of Fig. 4b, node H/V is expressed relative to those stations, which define the baseline as a ratio of one. [d]Calculated as height/half base width from Table 1. [e]Calculated as center of mass height/half base width from Table 1.

## 4 H/V Results Using All Available Hourly Data

Fig. 3a shows locations of the 12 3C HVO network stations that provide H/V from permanent, well-coupled sensors installed below grade in vaults or shallow boreholes at sites within Kīlauea caldera (Fig. 3b). Averaged in the log domain across the 12 stations, the per-station $\ln$ mean H/V curves define a network baseline H/V curve (a function of frequency) for comparison to H/V calculated from nodes located on ground surfaces (Fig. 4). These permanent network stations are distinct from the 71 surface-deployed HVO SS 0.2 Hz broadband nodes in the 2023 array (Table 2); we use "HVO network stations" for the former and "HVO SS 0.2 Hz nodes" for the latter throughout. The frequency of maximum H/V amplitude at HVO station UWE occurs at 25 Hz, which is likely spurious due to the leveling feet of the STS2 sensor chattering on the concrete pedestal pier (ANSS Technical Integration Committee, 2002), rather than a site response. Excluding this artifact, none of the 12 HVO network stations has a maximum H/V site response at frequencies exceeding 6 Hz.

Fig. 4a compares $\ln$ mean H/V for all node types with the 12 HVO network stations operating within the deployment extent. H/V at frequencies $> 2$ Hz scales proportionally with wind sensitivity, as predicted by Table 2 relative to the permanent HVO network stations (Fig. 4b). EPIC SS spiked 5 Hz 3C nodes installed in volcanic tephra (H/V from this subset of nodes is shown in Fig. 4a) represent most of the increased $\ln$ mean H/V at frequencies of 1 Hz to 10 Hz relative to the EPIC SS 5 Hz bucket nodes. Most commonly EPIC SS 5 Hz nodes have H/V that increases to maximum H/V at frequencies $> 20$ Hz (Supplemental Fig. S1). Consistent with the coupling-resonance behavior reported for poorly coupled sensors (Dean and Grant, 2024), the EPIC SS spiked 5 Hz 3C nodes exhibit a 12–35 Hz spike resonant peak of H/V (Supplemental Figs. S2–S4) absent from H/V of EPIC SS bucket nodes embedded in coral sand (Supplemental Fig. S5), also absent from the other, lower profile nodes deployed on tripartite leveling legs, including the GTI U3 2 Hz nodes (Supplemental Fig. S6), the HVO SS 0.2 Hz nodes (Supplemental Fig. S7), and the 12 permanent HVO network stations (Fig. 3b). Two factors likely contribute to the elevated horizontal-component H/V of the spiked nodes. First, even where the spike is well coupled to the surrounding surficial deposits, the horizontal response can be dominated by a resonance governed by the soil stiffness acting over the dimensions of the spike. Second, the spike can progressively decouple from the soil, or "float," which is itself a coupling phenomenon that can degrade the horizontal-component response over time.

Fig. 5 shows substantial variability in EPIC SS 5 Hz spiked-node H/V arising from spike resonances, strong wind sensitivity at higher frequencies, variable low-frequency noise, and, less commonly, near-complete decoupling from ground motion. These categories are distinguished in the H/V itself: spike resonances appear as narrow peaks at characteristic frequencies, strong wind sensitivity elevates the higher-frequency H/V, and low-frequency noise is confined to the low band, whereas near-complete decoupling produces anomalously low, broadband H/V that departs from the rest of the spiked-node population. Most EPIC SS 5 Hz spiked 3C nodes exhibit maximum H/V amplitudes at frequencies $> 15$ Hz. In contrast, HVO network stations dominantly have maximum H/V amplitudes at frequencies of $\sim$0.4 Hz to $< 1.5$ Hz, with a dominant mode of 0.6 Hz.

Most GTI U3 2 Hz nodes have maximum H/V at frequencies of $\sim$0.4 Hz to 1.5 Hz, similar to the HVO network stations (Fig. 4a). The HVO SS 0.2 Hz nodes have three dominant modes in the frequency of maximum H/V: 0.11 Hz (the low-frequency limit of the H/V calculations), 1.2 Hz, and 40 Hz (the maximum frequency of the H/V calculations) (Fig. 4a). EPIC SS 5 Hz bucket 3C nodes lack the high-frequency resonant response of EPIC SS 5 Hz spiked nodes and exhibit reduced wind amplification above 1.5 Hz (Fig. 4a).

Several of these results can be compared directly with Janiszewski et al. (2024), who deployed 80 surface SmartSolo IGU-BD3C-5 nodes (the instrument used here as the HVO SS 0.2 Hz node) in 2022 alongside many of the same HVO network stations. Three findings are consistent. They attribute elevated summit-station noise to near-constant volcanic tremor at 1–5 Hz, the same band and source identified here; their surface nodes are noisier than below-grade permanent sensors preferentially on the horizontal components, and their surface-installed permanent broadband sensors have more noise at long periods than vault, buried, or borehole installations, both consistent with rocking of poorly coupled surface sensors; and their IGU-BD3C-5 horizontal noise rises steeply at periods approaching and beyond the 5 s response corner, matching the increase in HVO SS 0.2 Hz node H/V from 0.3 Hz to 0.11 Hz seen here and absent from the other node types (Fig. 4a). Their inference that wind is probably not a significant noise source appears configuration-specific rather than gen-

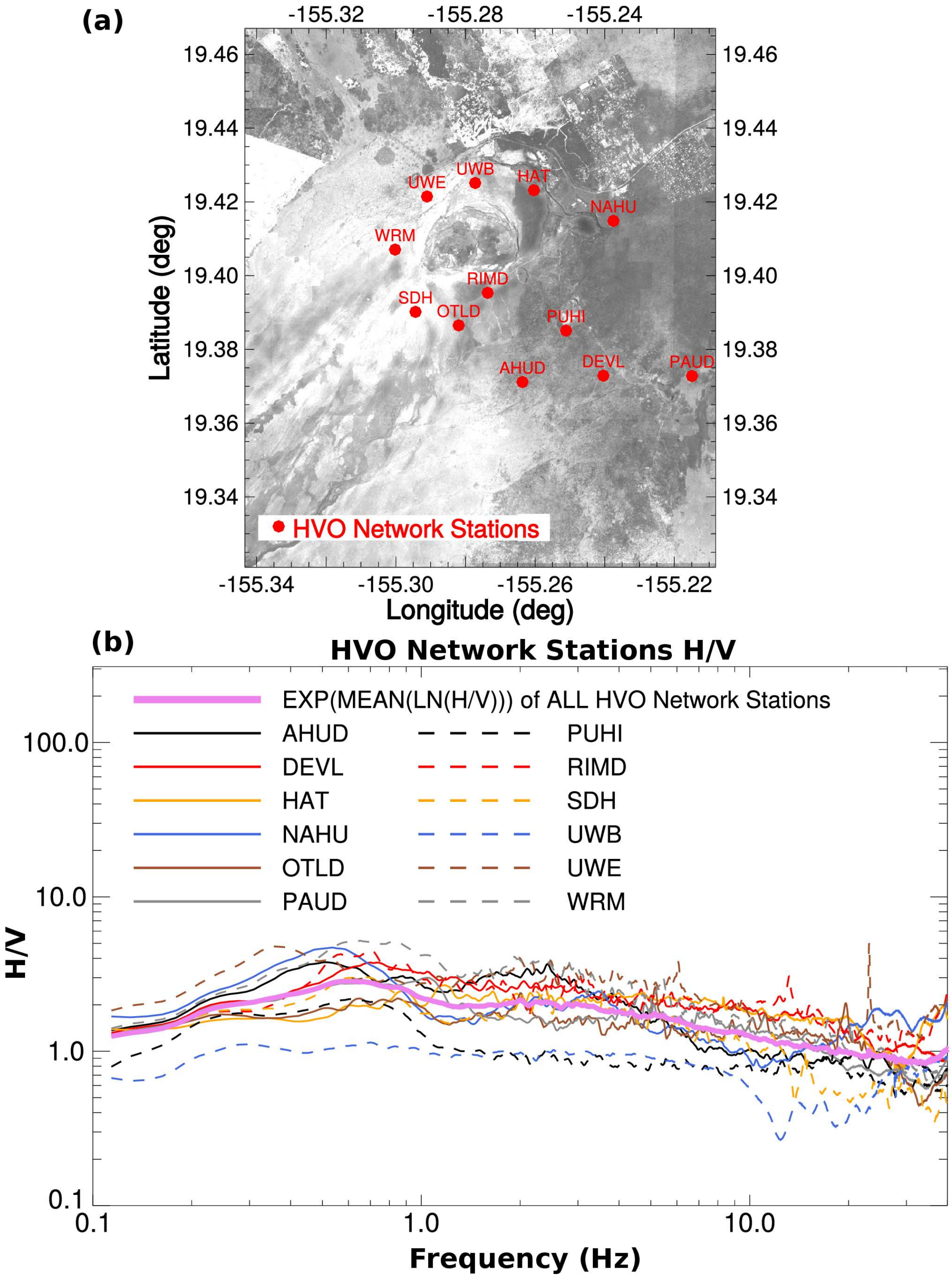


**Figure 3** (a) Map showing the 12 HVO network 3C stations operating during, and within the extent of, the 2023 Kīlauea nodal deployment. (b) Individual station H/V calculated from all available complete hours of data during the experiment as per the legend, with the $\ln$ mean H/V of all 12 stations as the thick solid magenta line.

eral: their nodes were low-profile, sandbag-loaded, unspiked, and situated in accumulated soil selected for shelter, whereas the grid geometry here required placement regardless of exposure with most nodes having taller spiked units. In this case, wind sensitivity scales with node shape (Table 2). Total-power comparisons also combine site, source, and instrument effects across both components, whereas H/V conditioned on wind speed isolates the horizontal degradation that rocking produces. Janiszewski et al. (2024) called for a direct comparison of instrument types and installation methods under common conditions: the four surface configurations and 12 below-grade network stations examined here provide one, and they support the choice of sandbag loading without spikes, since the spiked nodes here develop 12–35 Hz resonances and progressive horizontal decoupling that the bucket and leveling-leg deployments do not.

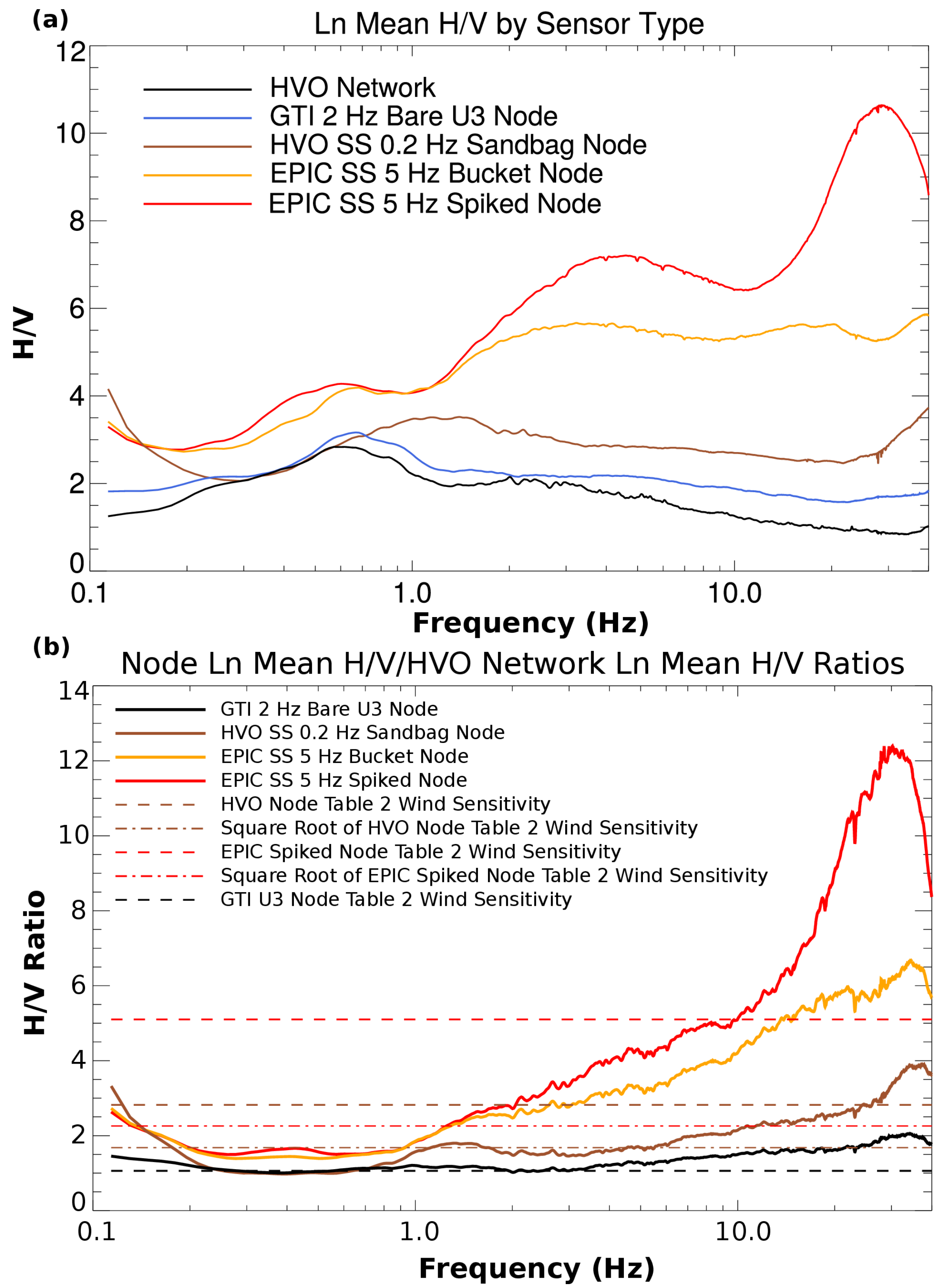


**Figure 4** (a) All available hour $\ln$ mean H/V as a function of sensor and/or node type and deployment configuration as per the legend. (b) Ratio of node $\ln$ mean H/V relative to HVO network $\ln$ mean H/V (solid lines) with wind sensitivity ratio estimates from Table 2 as dashed-dotted lines as per the legend.

## 5 H/V Sensitivity to Wind Speed Using Renormalized H/V And Hourly Wind Speed Data

The effects of variable and increasing low-frequency biases with increasing node wind sensitivity are illustrated in Figs 4 and 5. To facilitate identification of subsets of node data useful for site-response estimation and S-wave arrival-time picking, a simple H/V renormalization was used to eliminate low-frequency noise H/V amplification and to determine effective minimum frequencies of useful H/V S/N for each node type and deployment configuration (Supplemental Table S1).

Typical alternatives to this type of H/V renormalization include high-pass filtering with a 0.1–0.3 Hz corner frequency to remove low-frequency noise prior to H/V estimation; however, this would remove information on low-frequency S/N, so it was not implemented here. High-pass filtering with a 4.0–5.0 Hz corner frequency is usually necessary to enhance S-wave S/N for

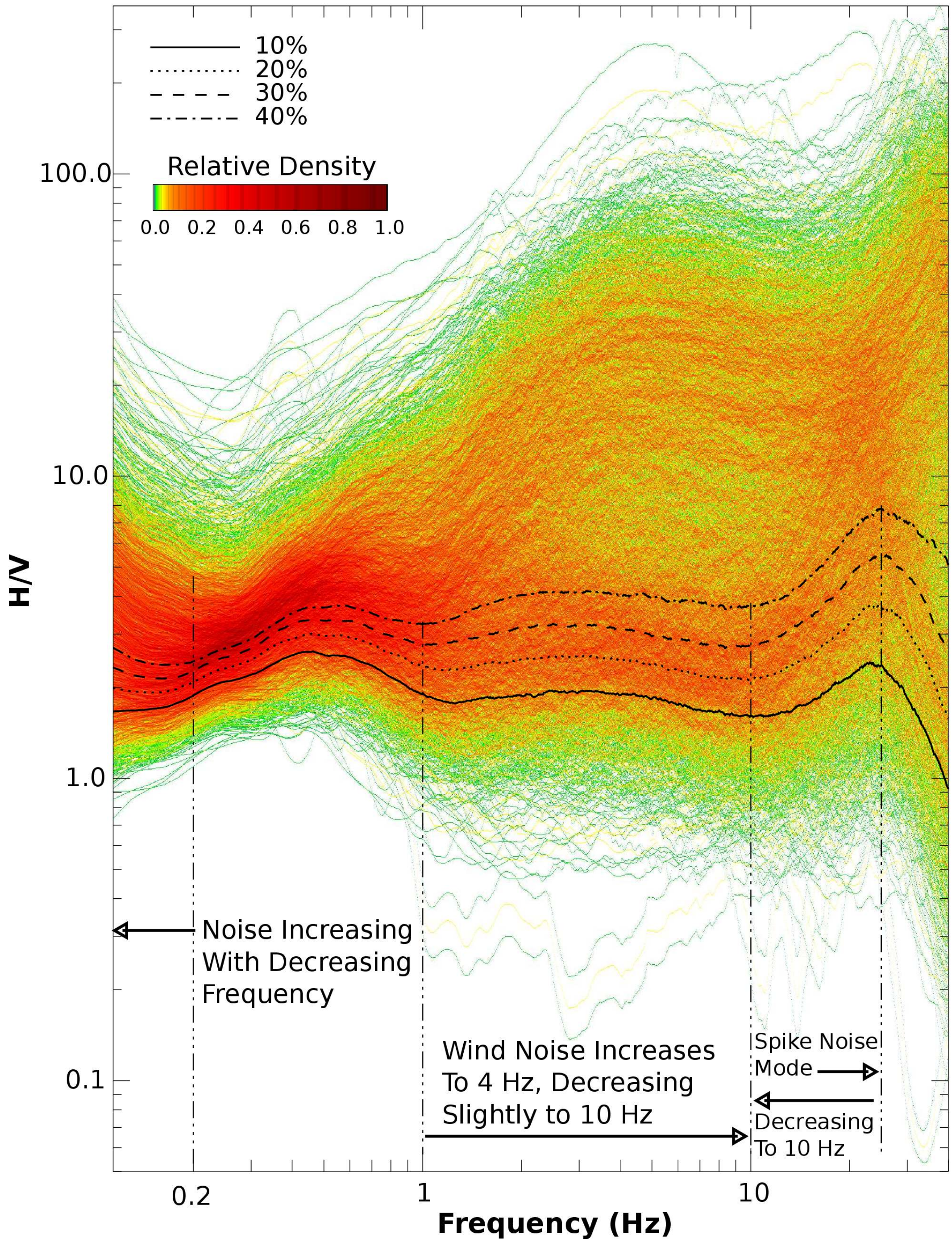


**Figure 5** All hour H/V relative density from all 1409 spiked EPIC SS 5 Hz nodes, with black lines showing the lower percentiles as a function of frequency as per the top legend and the colors denoting relative H/V density as per the color bar.

arrival-time picking of smaller-magnitude earthquakes, as previously discussed.

To obtain robust estimates of each station's H/V for low, median, and high wind speeds, processing was performed as follows. First, all 59 estimates of H/V obtained from each hour using non-overlapping 61.33 s windows are normalized to the H/V values at the normalization-frequency tie points in Supplemental Table S1. Weights for each of the 59 window H/V estimates within an hour are proportional to the cross-correlation of each window's H/V with the raw $\ln$ mean H/V for that hour. The cross-correlation (CC) range is rescaled to 0.01–1.0 to derive weights for the CC-weighted hourly H/V estimate. To produce the summary H/V for each node, the inverses of the H/V amplitude ratios (AR) (median 5.0–10.0 Hz H/V divided by median 1.0–2.0 Hz H/V) from each hourly H/V estimate are used to produce the weighted $\ln$ mean node CC-AR H/V.

Supplemental Figs. S8 and S9 contrast H/V responses between a low-profile node (the GTI U3 2 Hz node on leveling legs) and an EPIC SS 5 Hz bucket node, both deployed on relatively flat lava flows exposed to persistent trade winds. A subset of GTI U3 nodes in area 700 exhibit wind-speed noise sensitivity in H/V beginning between 1 Hz and 2 Hz, with peak wind-speed H/V approaching the peak lower-frequency site amplification in several cases (Supplemental Fig. S8c). The bucket nodes, having a larger wind cross-section than the GTI

U3 nodes, exhibit greater wind-speed noise sensitivity at frequencies $> 1$ Hz, often with maximum wind-noise amplification at frequencies $> 10$ Hz (Supplemental Fig. S8c). Bucket nodes also exhibit stronger H/V noise at frequencies $< 0.2$ Hz than the lower-profile GTI nodes. GTI node area 1500 was located in a narrow channel that locally amplified wind speed and showed the most adverse wind-noise impacts on H/V among the GTI deployment areas (Supplemental Fig. S9), with most nodes exhibiting increased H/V at frequencies $> 1$ Hz (Supplemental Fig. S9c). Bucket nodes on the adjacent hill west of the area 1500 GTI nodes (Supplemental Figs. S9a and S9b) also showed strong wind amplification beginning at frequencies as low as 0.6 Hz. Under sufficiently strong persistent winds, horizontal-component noise can dominate surface deployments of low-profile nodes on leveling bolts or nodes installed in buckets (Supplemental Fig. S9). Additional examples of wind-noise and site-condition effects on H/V and horizontal-component S/N are provided in the Supplement.

Further examples of EPIC SS 5 Hz spiked-node H/V sensitivity to wind speed are provided in the Supplement using both normalized and all-hour $\ln$ mean H/V. Examples include a node with moderate wind-speed sensitivity at frequencies $> 1$ Hz (Supplemental Fig. S10a), a node with strong wind-speed sensitivity at frequencies $> 0.8$ Hz (Supplemental Fig. S10b), a node with wind-speed-dependent horizontal-component ground decoupling (Supplemental Fig. S11a), near-complete horizontal-component ground decoupling at frequencies $< 10$ Hz (Supplemental Fig. S11b), moderate spike-resonance noise extending below 10 Hz (Supplemental Fig. S12a), and ambiguous H/V modes that may reflect site response or spike resonance (Supplemental Fig. S12b).

Although no nodes were co-sited with HVO network stations, two GTI U3 2 Hz nodes and eight EPIC SS 5 Hz spiked nodes were located within one nominal node spacing of HVO network stations. The Supplement contains node–HVO network H/V comparisons, including Supplemental Figs. S13 and S14 (all-hour $\ln$ mean H/V from the two GTI U3 2 Hz nodes paired with the closest HVO stations) and Supplemental Figs. S15–S22 (the corresponding comparison for the eight EPIC SS 5 Hz spiked nodes). Supplemental Figs. S15–S22 provide examples of wind-noise amplification at EPIC SS 5 Hz spiked nodes and illustrate the tendency for stations west and southwest of Kīlauea caldera to exhibit the strongest H/V sensitivity to wind noise.

## 6 Station Subsets with Relatively Low Wind Sensitivity and Spike Resonance Noise

For each nodal station, H/V curves from all complete hours were overlaid for three wind-speed cases ($<1.45$ m/s, 4.5 m/s [9-knot median wind speed], and $> 6.68$ m/s) to interactively pick frequency bandwidths with acceptable horizontal-component S/N and to identify stations meeting four S/N criteria. Stations with H/V that is stationary with respect to wind speed over frequency bands of interest were flagged and compiled into station lists, with each station's bandwidth of stationary H/V cataloged. For frequencies extending to at least 10 Hz, three station lists were created because the 486-station lowest-noise catalog represents only about 27% of all stations and is dominated by stations near roads or within Kīlauea Caldera. To consider a wider area, an intermediate 610-station catalog was used, including 124 stations that are likely noisier than those in the lowest-noise catalog. To further expand coverage to the west and southwest, a third 722-station catalog was used, including 113 stations that are somewhat noisier than those in the 610-station catalog.

To maximize spatial coverage, a 1,099-station list (Fig. 6a) was created by allowing wind-speed noise sensitivity that is often confined to frequencies above 1.2 Hz at most stations. An upper frequency of 1.2 Hz was used because horizontal-component S/N is likely adequate for interferometry over a broad portion of the 2023 Kīlauea node deployment, consistent with the use of high-corner-frequency nodes for ambient-noise and surface-wave imaging in the microseism band (Obermann et al., 2022). Some stations, particularly EPIC SS 5 Hz spiked nodes, exhibit increasing wind-speed noise sensitivity at frequencies $> 1$ Hz (Fig. 6b). Nevertheless, nearly all stations in the 1,099-station list have sufficiently low wind-speed noise sensitivity to support interferometry using horizontal-component data from 0.2–0.3 Hz to 1.2 Hz (Fig. 6b). Nearly all nodes, except the HVO SS 0.2 Hz nodes, have good horizontal-component S/N down to 0.2 Hz or lower (Fig. 6b). Many HVO SS 0.2 Hz nodes have strong noise at frequencies $< 0.3$ Hz, with H/V increasing as frequency decreases, particularly under median wind speeds (Fig. 6b; Supplemental figures). This behavior is reflected in a slight increase in HVO SS 0.2 Hz node $\ln$ mean H/V from 0.3 Hz to 0.2 Hz, whereas $\ln$ mean H/V decreases over the same band for the other node types and deployment configurations in Fig. 6b.

For S-wave arrival-time picking, moment-tensor inversion, and waveform-modeling analyses, three station subsets were identified with reduced wind-speed noise sensitivity and/or reduced spike-resonance responses that minimally degrade H/V and horizontal-component S/N at frequencies extending to at least 10 Hz. These station lists are provided in the supplemental material. The 722-station subset has modest or minimal wind sensitivity and spike-resonance noise to at least 10 Hz; most excluded stations are EPIC SS 5 Hz spiked nodes and bucket nodes located west and southwest of Kīlauea caldera (compare Fig. 6c to Fig. 1). The most notable increase in wind-speed noise sensitivity is reflected in increased $\ln$ mean H/V for EPIC SS 5 Hz spiked nodes near 2 Hz (Fig. 6d). Because site H/V resonances between 2–10 Hz are possible, some of the 113 nodes included in this subset (but not in the lower- or lowest-noise subsets) may capture dominant 2–10 Hz site-response H/V maxima or may be dominated by 2–10 Hz wind noise, which represents a fundamental limitation of this dataset.

Two smaller station subsets are provided with re-

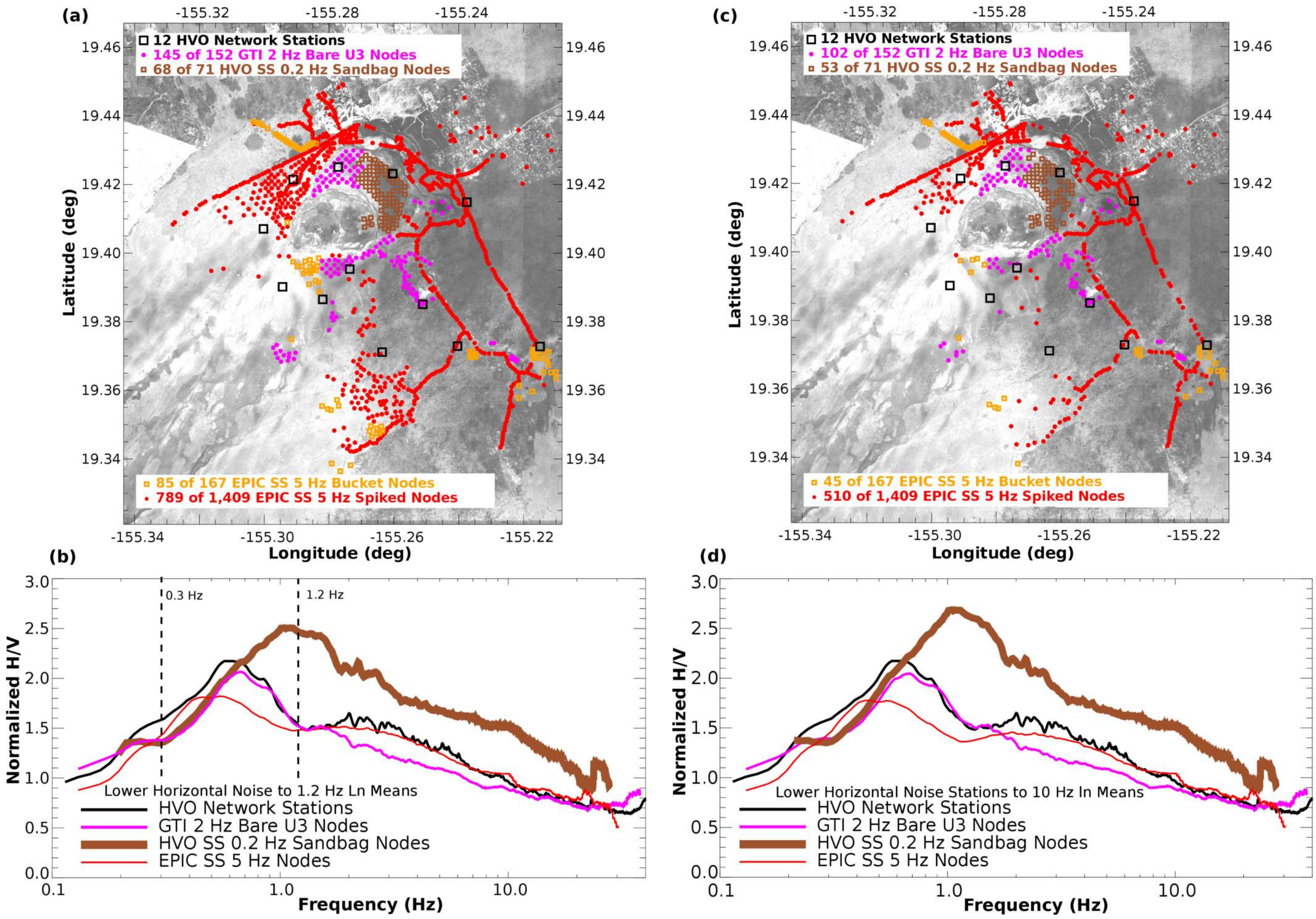


**Figure 6** (a) Location of the 1,099 stations with mostly low horizontal-component noise to at least 1.2 Hz, with station type indicated by colors and symbols in the legends. (b) Normalized all hour ln mean H/V for each station type from (a) as per the legend. (c) Location of the 722 stations with mostly low horizontal-component noise to at least 10 Hz, with station type indicated by colors and symbols in the legends. (d) Normalized all hour ln mean H/V for each station type from (c) as per the legend.

duced and minimal wind-speed noise sensitivity. To maximize station extent while limiting wind and spike-resonance noise at frequencies $< 10$ Hz, a 610-station subset provides coverage to the west and southwest (Fig. 7a) without strong increases in wind-speed noise sensitivity or spike-resonance noise (Fig. 7b). The 486-station minimum-horizontal-noise subset includes few stations in overland areas far from roads (Fig. 7c) but provides the best H/V S/N and the lowest wind-speed noise sensitivity at frequencies $> 2$ Hz (Fig. 7d), relative to the 610-station subset. The 486-station subset is recommended as a starting dataset for tuning and/or training S-wave arrival-time pickers; methods developed on this subset may help recover usable picks from larger, noisier station sets and thereby improve geographic coverage.

The lower (Fig. 7a) and lowest (Fig. 7c) wind-speed-noise-sensitivity subsets tend to occur along roads that are either sheltered by dense vegetation or underlain by graded road base on shoulders hosting EPIC SS 5 Hz spiked nodes. These road shoulders likely provided stiff ground conditions that minimized spike-resonance amplitudes and/or shifted spike-resonant frequencies high enough to limit impacts on H/V and horizontal-component S/N below 10 Hz. The supplemental material provides a list of 15 EPIC SS spiked nodes that appear to be decoupled from horizontal ground motion. These stations may still exhibit detectable S-wave arrivals, but horizontal ground-motion amplitudes may be unreliable. Nearly all 15 stations are located within dense nodal deployment areas with nearby stations exhibiting good horizontal-component coupling, low wind-speed sensitivity, and good horizontal-component and H/V S/N.

The long-period band used in regional moment-tensor practice lies well below the response corners of all node types deployed here, so moment-tensor analysis with this dataset is anticipated to rely on far-field body-wave observations rather than long-period waveform fitting. Methods of this class, such as the NaNDC algorithm of Yang and Wang (2025), jointly invert P-wave polarities, P-wave amplitudes, and S/P amplitude ratios for full moment tensors of small earthquakes recorded by dense nodal arrays, and Xin et al. (2026) applied it to 29 SmartSolo IGU-16HR 3C nodes using a 4–30 Hz passband. That band coincides with the band in which S-wave arrivals are detectable here, so the 722-, 610-, and 486-station subsets are the relevant station selections, and the S/P ratios are three-component measurements that depend on faithful horizontal amplitudes rather

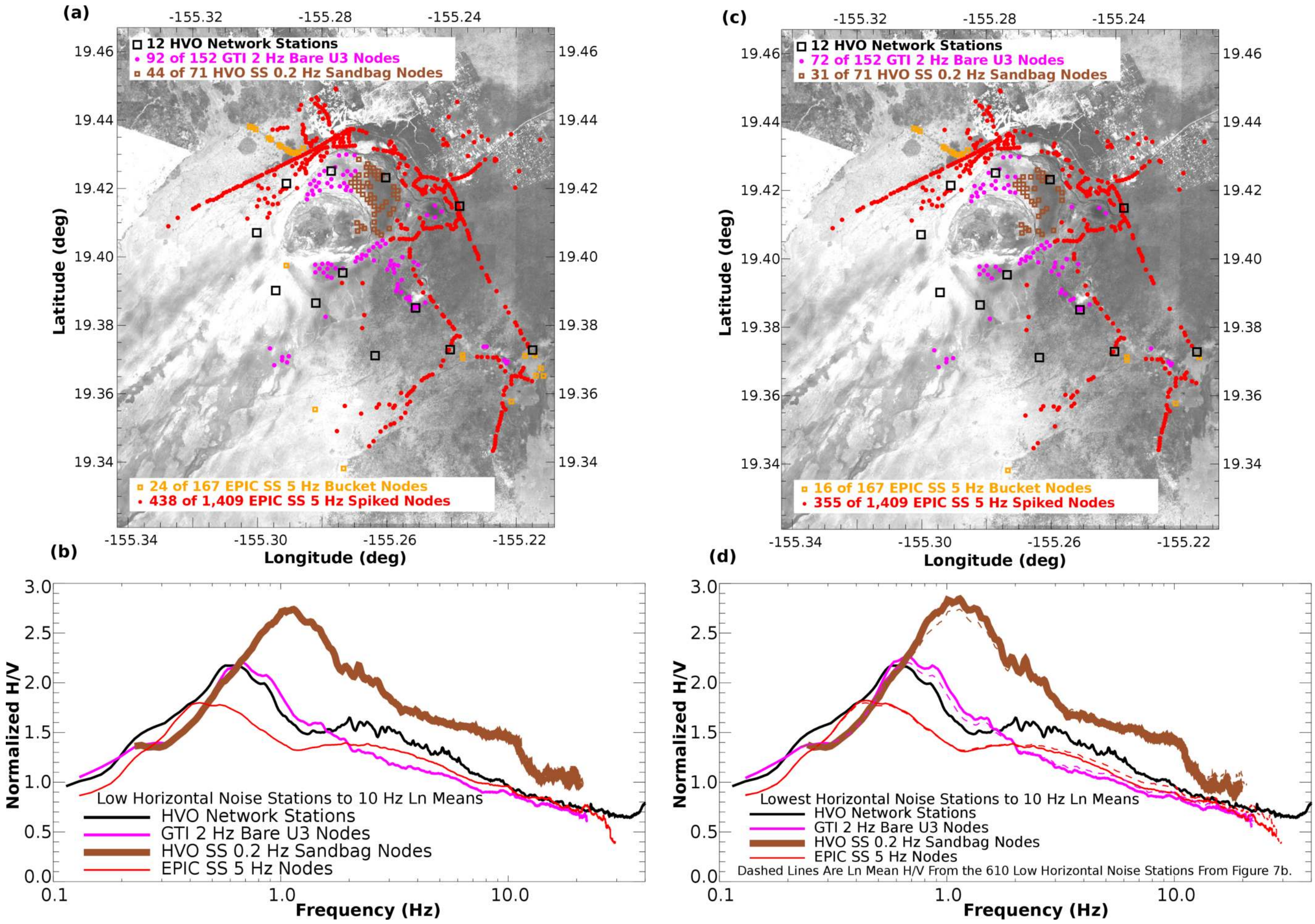


**Figure 7** (a) Location of the 610 stations with lower horizontal-component noise to at least 10 Hz, with station type indicated by colors and symbols in the legends. (b) Normalized all hour ln mean H/V for each station type from (a) as per the legend. (c) Location of the 486 stations with lowest horizontal-component noise to at least 10 Hz, with station type indicated by colors and symbols in the legends. (d) Normalized all hour ln mean H/V for each station type from (c) as per the legend, with the 610-station subset H/V from (b) overlaid as dashed lines for comparison.

than absolute calibration. Two features of this dataset bear directly on such an application. Xin et al. (2026) buried the same node model at roughly 20 cm, whereas permits precluded burial here, so station selection by H/V S/N substitutes for burial and the 15 horizontally decoupled nodes listed in the Supplement should be excluded. In addition, a 4–30 Hz passband would span the 12–35 Hz spike resonances documented in Section 4 for EPIC SS 5 Hz spiked nodes, which would bias P and S amplitudes at affected stations; the 610- and 486-station subsets were constructed to exclude nodes whose spike resonances extend below 10 Hz (Supplemental Fig. S23), and restricting the passband accordingly is advisable. Lower-frequency point-source waveform inversion remains possible on the 1,099-station subset from about 0.25 Hz to 1.2 Hz, subject to 1–5 Hz volcanic tremor and to the accuracy of Green's functions in a strongly heterogeneous shallow edifice.

# 7 Example of a Strategy for Surface Deployment of 3C Nodes on Loose Materials

A primary challenge was deploying nodes on loose materials while minimizing wind noise and spike-resonance noise, most commonly on volcanic tephra in the 2023 Kīlauea experiment. The tephra-deployment approach used in GTI deployment area 800 (Fig. 8a) illustrates a strategy that yielded broadband (0.2–40 Hz) H/V and component S/N on loose tephra (Fig. 8b). For most GTI U3 2 Hz stations in Fig. 8a, nodes were placed directly on tephra. Loose tephra was hand-swept to the side to expose a less loose, often moist and nearly level surface, usually only 1–4 cm below original ground, and nodes were pressed down and rotated to orient and level them. A small amount of tephra was then pushed against the low sides of the GTI U3 2 Hz nodes to reduce wind coupling (the sides of the GTI U3 2 Hz node are about 1 cm high; Fig. 2c). In practice this amounted to banking whatever loose tephra was available around the base of each node, which at many sites was thin or patchy and limited how much could be packed. More generally, the guiding practice was to seat each node in

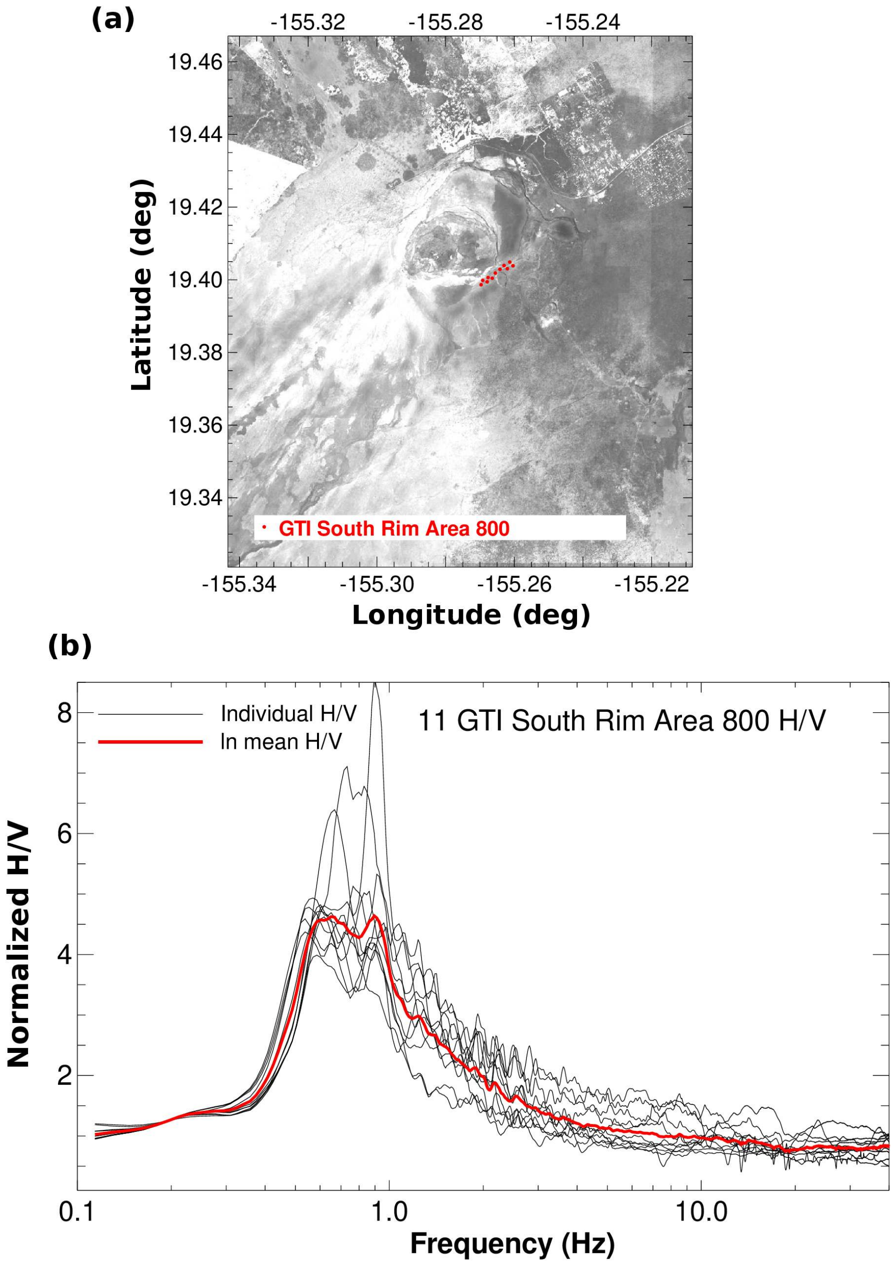


**Figure 8** (a) Location of 11 GTI U3 South Rim Area 800 stations placed on volcanic tephra. (b) Individual all hour ln mean H/V in black curves from the 11 GTI U3 stations in (a) with the ln mean H/V from these 11 stations (red curve).

soil or tephra rather than directly on solid basalt wherever the surface allowed, since loose material is far easier to level into and damps wind-induced rocking better than a hard, irregular rock contact. After node removal, the tephra was re-leveled by hand, restoring the sites to pre-deployment conditions. A similar strategy can be used for other nodes with low height-to-width ratios and flat bottoms after removing spikes or leveling legs. GTI U3 2 Hz nodes in area 800 along the southern rim of Kīlauea Caldera recorded T-REX vibroseis shear-mode first S-wave arrivals at the largest offsets ($>$ 7 km) of any nodes in the 2023 Kīlauea deployment. Other nodes did not yield observable S-wave arrivals from T-REX vibroseis shear-mode sourcing at offsets exceeding 3 km.

## 8 Conclusions

For larger earthquakes ($M > 2.5$) during the 2023 Kīlauea nodal deployment, S-wave arrivals are observed on most nodal stations. For smaller earthquakes and other passive applications, four station-subset lists are provided in the Supplement that likely have sufficient horizontal-component S/N to serve as starting points for interferometric, H/V, S-wave arrival-time picking, and moment-tensor analyses. These station subsets are intended as a quality-controlled foundation for horizontal-component analyses rather than as demonstrations of any single method. Prior characterizations of horizontal-component node performance have largely been confined to single instrument types or small deployments (Ringler et al., 2018; Johnson et al., 2019; Zeckra et al., 2022; Dean and Grant, 2024; Janiszewski et al., 2024), whereas the 2023 Kīlauea deployment allows horizontal-component S/N to be compared across permanent broadband sensors predominantly installed below grade in vaults or shallow boreholes (HVO network), with surface deployment of multiple node designs under a common, wind-dominated set of field conditions. The resulting subsets are meant to enable method-focused follow-on studies, for example automated S-wave arrival-time picking with formal uncertainty estimates, moment-tensor inversion, S-wave attenuation tomography, and ambient-noise interferometry, applied selectively to the instrument packages and frequency bands where horizontal-component S/N is adequate. Such method tests are beyond the length available here but are directly supported by the station lists and H/V S/N estimates provided in the Supplement. Passive attenuation estimation from temporary three-component nodal arrays remains uncommon. Liu et al. (2022) provide one example, recovering Love- and Rayleigh-wave attenuation across the San Jacinto fault from ambient-noise interferometry on a linear array of 65 three-component nodes, with the Love-wave result, which depends entirely on horizontal-component amplitudes, resolving an asymmetric damage zone. Both routes to attenuation available with the present dataset place demands on horizontal-component amplitude fidelity. Interferometric surface-wave attenuation of the kind used by Liu et al. (2022) requires stable horizontal amplitudes within the interferometry band, supported here by the 1,099-station subset from about 0.25 to 1.2 Hz. Body-wave S-wave spectral attenuation instead requires reliable amplitudes across the fitted band, where wind-driven horizontal noise and spike resonances both bias the result and the 486-station subset is the appropriate starting point. Some stations in these subsets still exhibit periods of elevated horizontal-component noise, primarily due to the wide range of wind speeds during the deployment and magma-inflation noise leading to the 7 June 2023 eruption. Additional transient (but often strong) daytime noise sources include low-altitude helicopters and fixed-wing aircraft, as well as vehicle traffic. These results are also intended to help inform selection of equipment for future node deployments to account for logistical constraints to maximize horizontal-component S/N.

## Acknowledgements

This work was supported by the 2019 Congressional supplement to the USGS, the NSF-FRES Grant EAR-2218645/2218646, and NHERI at UT Austin (NSF Grant 2037900). Vantage Geophysical provided T-REX pre-survey source-point mapping GPS equipment. GTI nodes, tablets, three T-REX orientation and position GPS loggers, and 24-channel source signature recorder equipment were provided by the Marian and Edward Erdelyi Science Fund. We also thank two anonymous reviewers for their valuable input in making this manuscript more robust.

## Data and code availability

The nodal data analyzed here are distributed by the EarthScope Consortium as FDSN network 6F, the USGS active and passive seismic interferometry experiment at Kīlauea volcano (Denlinger et al., 2023), DOI https://doi.org/10.7914/gqdb-hs97, released November 30, 2025. These data are archived in PH5 and are therefore retrieved through EarthScope's PH5 web services (`ph5ws`) or the federated catalog rather than the standard `fdsnws` endpoints at https://service.iris.edu; because the code 6F has also been used by unrelated deployments, requests should be restricted to the 2023 epoch. The 71 HVO SmartSolo SS 0.2 Hz nodes are archived separately under FDSN network code 8M (Kil_Act_HVOnodes), DOI https://doi.org/10.7914/fnv9-9r38 (Bennington et al., 2023), as part of the same 2023 experiment. Permanent station data are available under FDSN network code HV (HVO) (USGS Hawaiian Volcano Observatory, 1956), and the analysis code is available from O'Connell (2026). The earthquake catalogue derived from the experiment is available from Roecker et al. (2026).

## Competing interests

The authors declare no competing interests.

## References

ANSS Technical Integration Committee. Technical guidelines for the implementation of the Advanced National Seismic System. Technical Report Open-File Report 2002-92, U.S. Geological Survey, 2002. doi: 10.3133/ofr0292.

Bennington, N., Denlinger, R., Lin, G., Roecker, S., and O'Connell, D. Kil_Act_HVOnodes [Data set], 2023. doi: 10.7914/fnv9-9r38.

Dean, T. and Grant, M. A beginner's guide to seismic sensors. *Preview*, 2024(230):38–44, 2024. doi: 10.1080/14432471.2024.2395647.

Dean, T., Shem, A., and Al Hasani, M. Methods for reducing unwanted noise (and increasing signal) in passive seismic surveys. *ASEG Extended Abstracts*, 2018(1):1–7, 2018. doi: 10.1071/ASEG2018abW8_2A.

Denlinger, R., Lin, G., Haney, M., Roecker, S., Bennington, N., Flinders, A., O'Connell, D., and Vinarski, E. Active and passive seismic interferometry of Kīlauea volcano [Data set], 2023. doi: 10.7914/gqdb-hs97.

Dybing, S. N., Ringler, A. T., Wilson, D. C., and Anthony, R. E. Characteristics and Spatial Variability of Wind Noise on Near-Surface Broadband Seismometers. *Bulletin of the Seismological Society of America*, 109(3):1082–1098, 2019. doi: 10.1785/0120180227.

Farrell, J., Wu, S.-M., Ward, K. M., and Lin, F.-C. Persistent Noise Signal in the FairfieldNodal Three-Component 5-Hz Geophones. *Seismological Research Letters*, 89(5):1609–1617, 2018. doi: 10.1785/0220180073.

Garza, J. A., Chu, P.-S., Norton, C. W., and Schroeder, T. A. Changes of the prevailing trade winds over the islands of Hawaii and the North Pacific. *Journal of Geophysical Research: Atmospheres*, 117:D11109, 2012. doi: 10.1029/2011JD016888.

Geophysical Technology, Inc. NRU U3: 3-Component Seismic Recorder. https://www.geophysicaltechnology.com/nru-u3, 2026. Accessed: 2026-04-21.

Janiszewski, H., Bennington, N., and Wight, J. A Seismic Nodal Deployment to Understand Magmatic Structure in the Vicinity of the Pāhala Earthquake Swarm. *Seismological Research Letters*, 95(5):3082–3092, 2024. doi: 10.1785/0220240060.

Johnson, C. W., Vernon, F., Nakata, N., and Ben-Zion, Y. Atmospheric Processes Modulating Noise in Fairfield Nodal 5-Hz Geophones. *Seismological Research Letters*, 90(4):1612–1618, 2019. doi: 10.1785/0220180383.

Karplus, M. and Schmandt, B. Preface to the Focus Section on Geophone Array Seismology. *Seismological Research Letters*, 89(5): 1597–1600, 2018. doi: 10.1785/0220180212.

Lees, J. M. and Park, J. Multiple-taper spectral analysis: A standalone C-subroutine. *Computers & Geosciences*, 21(2):199–236, 1995. doi: 10.1016/0098-3004(94)00067-5.

Liu, X., Ben-Zion, Y., and Beroza, G. C. Ambient Noise Attenuation Tomography Reveals an Asymmetric Damage Zone Across San Jacinto Fault Near Anza, California. *Geophysical Research Letters*, 49, 2022. doi: 10.1029/2022GL099562.

Obermann, A., Sánchez-Pastor, P., Wu, S.-M., Wollin, C., Baird, A. F., Isken, M. P., Clinton, J., Goertz-Allmann, B. P., Dahm, T., Wuestefeld, A., Shi, P., Lanza, F., Gyger, L., Wetter, S., Hjörleifsdóttir, V., Langet, N., Brynjarsson, B., Jousset, P., and Wiemer, S. Combined Large-N Seismic Arrays and DAS Fiber Optic Cables across the Hengill Geothermal Field, Iceland. *Seismological Research Letters*, 93(5):2498–2514, 2022. doi: 10.1785/0220220073.

O'Connell, D. HVSR code for 2023 Kīlauea Horizontal-Component Signal/Noise Assessment of a Large Three-Component Nodal Array [software], Apr. 2026. doi: 10.5281/zenodo.19929263.

Parker, L. M., Thurber, C. H., Zeng, X., Li, P., Lord, N. E., Fratta, D., Wang, H. F., Robertson, M. C., Thomas, A. M., Karplus, M. S., Nayak, A., and Feigl, K. L. Active-Source Seismic Tomography at the Brady Geothermal Field, Nevada, with Dense Nodal and Fiber-Optic Seismic Arrays. *Seismological Research Letters*, 89 (5):1629–1640, 2018. doi: 10.1785/0220180085.

Peterson, J. R. Observations and Modeling of Seismic Background Noise. Open-File Report 93-322, U.S. Geological Survey, 1993. doi: 10.3133/ofr93322.

Ringler, A. T., Anthony, R. E., Karplus, M. S., Holland, A. A., and Wilson, D. C. Laboratory Tests of Three Z-Land Fairfield Nodal 5-Hz, Three-Component Sensors. *Seismological Research Letters*, 89 (5):1601–1608, 2018. doi: 10.1785/0220170236.

Roecker, S., Denlinger, R. P., and O'Connell, D. R. H. Seismic catalogue derived from the 2023 Kīlauea Seismic Imaging Experiment, Kīlauea, Hawai'i, USA. Data release, 2026. doi: 10.5066/P1WQ3UHP.

Schmandt, B. and Clayton, R. W. Analysis of Teleseismic P Waves with a 5200-Station Array in Long Beach, California: Evidence for an Abrupt Boundary to Inner Borderland Rifting. *Journal of Geophysical Research: Solid Earth*, 118(10):5320–5338, 2013. doi: 10.1002/jgrb.50370.

SmartSolo Inc. IGU-16HR 3C: 3 Component Smart Seismic Sensor. https://smartsolo.com/igu-16hr-3c.html, 2026a. Accessed: 2026-04-21.

SmartSolo Inc. IGU-BD3C-5: Broadband Integrated 3 Component Seismograph. https://smartsolo.com/igu-bd3c-5.html, 2026b. Accessed: 2026-04-21.

Smith, S. W. *The Scientist and Engineer's Guide to Digital Signal Processing*. California Technical Publishing, San Diego, CA, 1998.

Thomson, D. J. Spectrum estimation and harmonic analysis. *Proceedings of the IEEE*, 70:1055–1096, 1982.

Trow, A. J., Zhang, H., Record, A. S., Mendoza, K. A., Pankow, K. L., and Wannamaker, P. E. Microseismic Event Detection Using Multiple Geophone Arrays in Southwestern Utah. *Seismological Research Letters*, 89(5):1618–1628, 2018. doi: 10.1785/0220180065.

USGS Hawaiian Volcano Observatory. Hawaiian Volcano Observatory Network [Data set], 1956. doi: 10.7914/SN/HV.

Ward, K. M. and Lin, F.-C. On the Viability of Using Autonomous Three-Component Nodal Geophones to Calculate Teleseismic Ps Receiver Functions with an Application to Old Faithful, Yellowstone. *Seismological Research Letters*, 88(5):1268–1278, 2017. doi: 10.1785/0220170051.

Xin, L., Wang, R., He, L., Guo, Z., Yang, L., He, Z., and Zuo, D. Rapid Seismicity Monitoring After the March 2023 $M_s$ 4.5 Earthquake Around the Xinfengjiang Reservoir, China. *Seismological Research Letters*, 97(2A):822–831, 2026. doi: 10.1785/0220250262.

Yang, L. and Wang, R. NaNDC: Full Moment Tensor Inversion and Uncertainty Analysis for Large-N Monitored Small Earthquakes. *Seismological Research Letters*, 96(2A):1150–1162, 2025. doi: 10.1785/0220240219.

Zeckra, M., Van Noten, K., and Lecocq, T. Sensitivity, Accuracy and Limits of the Lightweight Three-Component SmartSolo Geophone Sensor (5 Hz) for Seismological Applications. EarthArXiv preprint, 2022. doi: 10.31223/X5F073. preprint, not peer reviewed.